

Examining the Mechanical Equilibrium of Microscopic Stresses in Molecular Simulations

Alejandro Torres-Sánchez, Juan M. Vanegas,* and Marino Arroyo†
LaCàN, Universitat Politècnica de Catalunya–BarcelonaTech, 08034 Barcelona, Spain

(Received 3 November 2014; published 23 June 2015)

The microscopic stress field provides a unique connection between atomistic simulations and mechanics at the nanoscale. However, its definition remains ambiguous. Rather than a mere theoretical preoccupation, we show that this fact acutely manifests itself in local stress calculations of defective graphene, lipid bilayers, and fibrous proteins. We find that popular definitions of the microscopic stress violate the continuum statements of mechanical equilibrium, and we propose an unambiguous and physically sound definition.

DOI: 10.1103/PhysRevLett.114.258102

PACS numbers: 87.10.Tf, 87.15.A-, 87.15.La, 87.16.D-

The stress $\boldsymbol{\sigma}(\mathbf{x})$ is a second-rank tensor field encoding the internal force distribution in a continuum system; when multiplied by a unit vector \mathbf{n} , it provides the forces per unit area in the material across a surface passing through \mathbf{x} and perpendicular to \mathbf{n} . The continuum stress field can be connected to the statistical mechanics of discrete particle systems, in what is called the microscopic stress. Today, the microscopic stress is increasingly used to recapitulate mechanical information contained in long molecular dynamics (MD) trajectories of nonuniform systems, or to connect molecular details with continuum physics at larger scales. Significant applications include defective bulk [1,2] and two-dimensional crystals [3,4], biomolecular assemblies such as lipid bilayers [5–7], membrane proteins [8,9], and even isolated molecules [10].

The average (or virial) stress of a periodic system can be uniquely defined and given a precise thermodynamical interpretation [11]. There are, however, multiple procedures to map a statistical mechanics ensemble into a stress field. This indeterminacy is expected since any divergence-free symmetric tensor field (self-equilibrated) can be added to the local stress without affecting the continuum statements of balance of linear and angular momentum for a system in equilibrium [12,13],

$$\sigma_{ij,j} = 0, \quad (1a)$$

$$\sigma_{ij} = \sigma_{ji}, \quad (1b)$$

where we have ignored externally applied force and torque densities. The ambiguity in the microscopic stress is widely appreciated theoretically, but its practical consequences have been largely overlooked, partly because different definitions coincide for simple force fields [7]. As molecular simulations model increasingly complex systems, the issue of whether different definitions of the microscopic stress satisfy the fundamental requirements of mechanical equilibrium in Eq. (1) has not been systematically examined.

Here, we simulate the equilibrium behavior of three important condensed matter systems—defective graphene, lipid bilayers, and coiled-coil fibrous proteins—using MD simulations with realistic atomistic force fields, and study

the significance of the definition of the microscopic stress. We consider the atomic virial stress [3,4,14] and several flavors of the Irving-Kirkwood stress [7,8,15–19]. Strikingly, we find that the atomic virial stress does not satisfy balance of linear momentum. Furthermore, we find that a widely used version of the Irving-Kirkwood stress [15] does not satisfy balance of angular momentum for systems with chiral constituents. Our results favor a recent canonical definition of the Irving-Kirkwood stress [16,17], which, however, is limited to multibody potentials with at most four-body interactions. Motivated by higher-body force fields used in materials science and biochemistry [20,21], we develop and test a new and general procedure [22] to uniquely obtain a physically meaningful microscopic stress.

Microscopic stress fields include a kinetic contribution $\boldsymbol{\sigma}_K$, describing the flux of momentum due to internal vibrations, and a potential contribution $\boldsymbol{\sigma}_V$, accounting for the interatomic forces. Since the difficulty in the microscopic stress definition stems from the potential part, we focus only on this contribution and refer to [23] for the expression of $\boldsymbol{\sigma}_K$. For solid systems, where atoms stay relatively immobile, it is common to resort to the atomic virial stress definition [14], which is conceptually and computationally simpler than other definitions. In this method, the potential component is computed by distributing the virial of each potential contribution equally among the particles involved. More specifically, let the potential of the system be described additively as $V = \sum_{I=1}^M V_I$, with each contribution involving n_I particles. Then, we have

$$\boldsymbol{\sigma}_V^\alpha = \frac{1}{\Omega_\alpha} \sum_{I \in \mathcal{I}^\alpha} \frac{1}{n_I} \left\langle \sum_{\beta} \frac{\partial V_I}{\partial \mathbf{r}^\beta} \otimes \mathbf{r}^\beta \right\rangle, \quad (2)$$

where \mathbf{r}^β is the position of particle β , \mathcal{I}^α collects the set of potential contributions involving particle α , and Ω_α is the volume of this particle.

An alternative definition of the microscopic stress with a more solid statistical mechanics foundation was pioneered by Irving and Kirkwood [34,35] for two-body potentials. This approach, which we label as IK, defines the stress at

each point in space, $\sigma(\mathbf{x})$, rather than at the particles, and is thus more popular in fluid systems. The IK microscopic stress is identified by invoking Eq. (1a), which is therefore satisfied *ab initio* [34,35]. The potential component at position \mathbf{x} is given by

$$\sigma_V(\mathbf{x}) = \left\langle \sum_{\alpha, \beta > \alpha} \mathbf{f}^{\alpha\beta} \otimes \mathbf{r}^{\alpha\beta} B(\mathbf{r}^\alpha, \mathbf{r}^\beta; \mathbf{x}) \right\rangle, \quad (3)$$

where $\mathbf{r}^{\alpha\beta} = \mathbf{r}^\beta - \mathbf{r}^\alpha$, $B(\mathbf{r}^\alpha, \mathbf{r}^\beta; \mathbf{x}) = \int_0^1 \delta[(1-s)\mathbf{r}^\alpha + s\mathbf{r}^\beta - \mathbf{x}] ds$ is the bond function [35], and $\delta(\mathbf{r}^\alpha - \mathbf{x})$ is the Dirac delta distribution centered at \mathbf{x} . For two-body interactions $V_I = V_{\alpha\beta}(r^{\alpha\beta})$, we have $\mathbf{f}^{\alpha\beta} = V'_{\alpha\beta} \mathbf{r}^{\alpha\beta} / r^{\alpha\beta}$, where $r^{\alpha\beta} = |\mathbf{r}^{\alpha\beta}|$. In practice, space is subdivided into a grid and the microscopic stress is evaluated at discrete positions [7].

There have been a number of extensions of the IK framework to deal with multibody potentials [12,15,16,18,19]. Some of these approaches fully retain balance of linear momentum by construction [12,15,16], by defining $\mathbf{f}^{\alpha\beta}$ as the terms of a pairwise force decomposition $\mathbf{F}^\alpha = \sum_\beta \mathbf{f}^{\alpha\beta}$ satisfying $\mathbf{f}^{\alpha\beta} = -\mathbf{f}^{\beta\alpha}$, with \mathbf{F}^α being the total force acting on particle α . The indeterminacy of the local stress tensor manifests itself in the IK definition because the pairwise force decomposition is not unique for potentials involving three or more particles. We consider initially the so-called central force decomposition (CFD) [13,16] and defer further discussion to later in this Letter.

We first consider a periodic graphene sheet with a Stone-Wales defect as a model system to compare the atomic virial and the IK stresses. The system is modeled with the force field described in [36] involving up to four-body interactions and simulated in a NVT ensemble at 300 K [23]. We compute microscopic stresses here and elsewhere in the Letter with a freely available implementation [7,37]. Figure 1(a) highlights the fundamental features of each stress definition. The atomic virial stress is defined discretely at the atoms, while the IK stress is continuous but exhibits marked concentrations along lines joining atomic positions, a signature of the force decomposition. It is often convenient to spatially average the discrete features in these fields with weighting functions such as Gaussian kernels [13,23,38]. Figure 1(b) shows that the spatially averaged fields $\bar{\sigma}$ according to both notions of stress are qualitatively similar, although the atomic virial stress exhibits smaller magnitudes.

We analyze next whether these fields are in equilibrium, as physically expected. Importantly, it can be shown by a simple calculation that $\bar{\sigma}_{ij,j}(\mathbf{x})$ is the spatial average of $\sigma_{ij,j}(\mathbf{y})$ [23]. Therefore, $\bar{\sigma}_{ij,j}$ should be zero if the corresponding microscopic stress σ_{ij} obeys Eq. (1a). Strikingly, the atomic virial stress is strongly out of equilibrium in the vicinity of the defect, Fig. 1(c). In contrast, the IK stress field exhibits nearly zero divergence (except from deviations due to discretization and limited statistical sampling). Thus, our results suggest that the atomic virial stress should be employed only for visualization purposes.

We focus next on the various extensions of the IK stress for multibody interactions. A generalization of the method

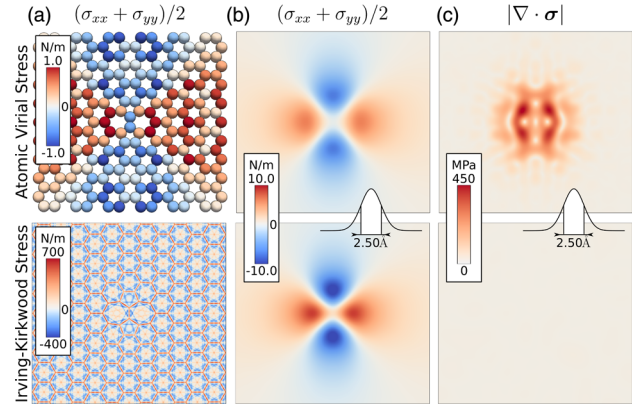


FIG. 1 (color online). Balance of linear momentum of the microscopic stress in a graphene sheet with a Stone-Wales defect: comparison of the atomic virial (upper row) and the IK (lower row) stress definitions. (a) Trace of the raw stress fields. (b) Spatially averaged trace of the stress field. (c) Norm of the divergence of the spatially averaged microscopic stress. Plots focus on a small region near the defect in the $x - y$ plane. Because the system is quasi-2D, we only consider the in-plane components and express stress in units of surface tension.

of planes has been proposed by Heinz, Paul, and Binder (HPB) [18,19], which is consistent with the IK stress for two-body potentials and also recovers the global virial stress. We find that this method does not exactly satisfy balance of linear momentum, albeit with a smaller error than the atomic virial stress [23]. We examine next other IK generalizations satisfying Eq. (1a) by construction. A natural force decomposition satisfying $\mathbf{f}^{\alpha\beta} = -\mathbf{f}^{\beta\alpha}$ was proposed by Goetz and Lipowsky [15],

$$\mathbf{f}_{\text{GLD}}^{\alpha\beta} = \sum_{I=1}^M \frac{1}{n_I} \left(\frac{\partial V_I}{\partial \mathbf{r}^\beta} - \frac{\partial V_I}{\partial \mathbf{r}^\alpha} \right). \quad (4)$$

This Goetz-Lipowsky decomposition (GLD) has been widely employed to analyze MD simulations ([5,7,8] and references therein), yet it produces noncentral forces; i.e., in general $\mathbf{f}_{\text{GLD}}^{\alpha\beta}$ is not parallel to $\mathbf{r}^{\alpha\beta}$. In principle, this could lead to nonsymmetric stresses [12,16]. Recently, a central force decomposition has been proposed by Admal and Tadmor [13,16], which produces a symmetric stress tensor by construction because $\mathbf{f}^{\alpha\beta}$ is defined such that it is always parallel to $\mathbf{r}^{\alpha\beta}$, see Eq. (3). By invariance with respect to rigid body transformations, the additive potential contributions can be represented in terms of interatomic distances, $\tilde{V}_I(r^{12}, \dots, r^{(n_I-1), n_I}) = V_I(r^1, \dots, r^{n_I})$, leading to the CFD pairwise forces

$$\mathbf{f}_{\text{CFD}}^{\alpha\beta} = \sum_{I=1}^M \frac{\partial \tilde{V}_I}{\partial r^{\alpha\beta}} \frac{\mathbf{r}^{\alpha\beta}}{r^{\alpha\beta}}. \quad (5)$$

The CFD and GLD force decompositions result in pairwise forces with large differences in magnitude and direction [23]. To explore the features of each force decomposition, we consider a lipid bilayer system of fluid DPPC

(1,2-dipalmitoyl-sn-glycero-3-phosphocholine), which is isotropic in the membrane plane ($x - y$) at the simulated temperature (323 K). In addition to the conventional profiles of all stress components across the thickness, we adopt an unconventional but intuitive method to visualize stress through the traction vector, $\mathbf{t} = \boldsymbol{\sigma} \cdot \mathbf{n}$, on a given internal surface with unit normal \mathbf{n} (Fig. 2). The traction can be decomposed into a normal and a tangential component, $\mathbf{t} = t_n \mathbf{n} + \boldsymbol{\tau}$. Here, we consider a test cylinder, and represent the normal traction t_n as a color map and the tangential component $\boldsymbol{\tau}$ using arrows.

In agreement with the symmetries of this system and the fluidity of the bilayer, the CFD stress is diagonal with equal lateral components ($\sigma_{xx} = \sigma_{yy}$) and a normal constant component across the bilayer [$\sigma_{zz}(z) = \text{const.}$] as dictated by Eq. (1a) [Fig. 2(a)]. We note that for a bilayer in the gel phase, the off-diagonal components could be nonzero but should nevertheless respect the symmetry of $\boldsymbol{\sigma}$. In sharp contrast, the GLD stress exhibits nonzero in-plane off-diagonal components, which are antisymmetric ($\sigma_{xy} = -\sigma_{yx}$) and of significant magnitude [Fig. 2(b)], hence violating Eq. (1b). Furthermore, CFD and GLD produce significantly different lateral components, and, hence, normal tractions ($t_n = \sigma_{xx} = \sigma_{yy}$) [Fig. 2(c)].

Focusing on the tangential traction, we note that $\boldsymbol{\tau}$ is parallel to the bilayer plane with sense and magnitude given

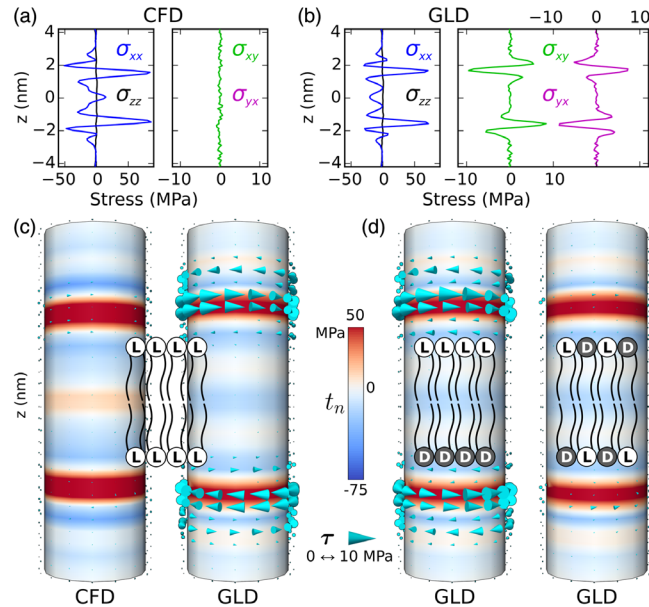


FIG. 2 (color online). Balance of angular momentum of the IK stress in a planar DPPC fluid membrane, and influence of lipid chirality. In-plane components of the stress tensor analyzed with CFD (a) and GLD (b). (c) Visualization of the normal and tangential components of the traction vector along a cylindrical surface perpendicular to the bilayer plane, for both CFD and GLD. The effect of the lipid chirality on the GLD stress for the two DPPC enantiomers, L-DPPC and D-DPPC, is shown in (d), where we consider a lipid membrane composed of monolayers with different chiralities (one with pure L-DPPC and the other with pure D-DPPC, left), and a bilayer with both monolayers having equal numbers of L-DPPC and D-DPPC (right).

by $\sigma_{xy} = -\sigma_{yx}$. As expected, for CFD $\boldsymbol{\tau}$ is nearly zero. For GLD, however, it is clear from Fig. 2(c) that the non-symmetry of the stress tensor introduces distributed torques of opposite sign in each leaflet of the bilayer, since $\sigma_{xy}(z) = -\sigma_{xy}(-z)$. We hypothesize that such behavior may be due to the internal structure of each lipid, since the headgroup portion of DPPC contains a chiral carbon. We test this hypothesis by comparing the stress tensors for three systems with different mixtures of the two DPPC enantiomers (L-DPPC and D-DPPC). Consistent with this hypothesis, the torques induced in each monolayer according to GLD adopt the same sign for a system with one monolayer composed solely of L-DPPC and the second monolayer composed solely of D-DPPC [Fig. 2(d)]. Mixing equal numbers of each chiral lipid in both monolayers results in nearly zero distributed torques according to the GLD stress. Thus, the off-diagonal components of the GLD stress tensor reflect the average chirality of the molecular composition. In contrast, we find that the CFD stress tensor is essentially unchanged by the lipid chirality [23].

To physically interpret the GLD distributed torques, it is necessary to resort to an extended theory of continuum mechanics. In micropolar continuum theories, these torques can be balanced locally by invoking a couple stress field \mathbf{m} , which in equilibrium satisfies $\epsilon_{ijk}^l \sigma^{jk} = \nabla_l m^{il}$, where ϵ_{ijk} is the Levi-Civita symbol [12,39–41]. In our situation, however, there is no compelling physical justification for this field since the primary objects of our model are achiral point particles [41] and there is no apparent external source for \mathbf{m} . Thus, although the connection between the non-symmetry of the IK-GLD stress and molecular chirality is very appealing, this example undermines its mechanical interpretation. The HPB stress [18,19] produces nonsymmetric stresses very similar to GLD for this system [23].

The microscopic stress tensor not only serves as a tool to explore the local distribution of forces, but can also provide important material properties. For instance, the Gaussian curvature modulus of lipid bilayers can be computed as $\bar{\kappa} = \int [(\sigma_{xx} + \sigma_{yy})/2 - \sigma_{zz}] z^2 dz$, which is highly sensitive to the features of the stress profile (see [6] and references therein). For the three bilayer systems with different chiralities in Fig. 2, we obtain $\bar{\kappa}_{\text{CFD}} = (-6.4, -6.7, -6.1) \times 10^{-20}$ J, in agreement with the common estimates of $\bar{\kappa}$ in the order of the negative of the bending modulus $\sim 5-15 \times 10^{-20}$ J [42]. Strikingly, we find $\bar{\kappa}_{\text{GLD}} = (0.91, 0.57, 1.3) \times 10^{-20}$ J, with the wrong sign—suggesting that a DPPC bilayer would be unstable [43]—and widely varying magnitudes.

Taken together, these results show that the choice of microscopic stress definition is not a mere theoretical preoccupation. Our results strongly favor the IK-CFD definition, which, unlike the atomic virial or the IK-GLD stresses, identically satisfies Eq. (1) for a system in equilibrium. However, CFD is not uniquely defined when $n_l > 4$. The geometric reason behind this ambiguity is that the $n_l(n_l + 1)/2$ interatomic distances ($r^{12}, \dots, r^{(n_l-1), n_l}$)

involved in a given multibody potential V_I cannot be arbitrarily chosen in $\mathcal{D}_I = \mathbb{R}_+^{n_I(n_I+1)/2}$. There are geometric conditions that make these distances realizable by a system of n_I particles, which define the so-called shape space $\mathcal{S}_I \subset \mathcal{D}_I$. When $n_I > 4$, the dimension of the manifold \mathcal{S}_I is smaller than $n_I(n_I + 1)/2$, and, therefore, the differential calculus involved in Eq. (5) needs to be carefully considered [44,45]. More practically, when $n_I > 4$ there are infinitely many different ways to express the potential, \tilde{V}_I , in terms of interatomic distances, each resulting in a different force decomposition and microscopic stress [13,16].

In the spirit of [46–48], we propose an alternative thermodynamic derivation of the IK microscopic stress, which naturally and unambiguously extends CFD to multi-body potentials. In analogy to the Doyle-Ericksen equation of continuum mechanics [49,50], the stress tensor can be defined from covariance arguments as

$$\sigma(\mathbf{x}) = \frac{2}{\sqrt{g(\mathbf{x})}} \frac{\delta A}{\delta \mathbf{g}(\mathbf{x})}, \quad (6)$$

where $g(\mathbf{x})$ is the Jacobian determinant of the metric and δA is the variation of the canonical free energy with respect to an infinitesimal change of metric $\delta \mathbf{g}(\mathbf{x})$ resulting from a change of coordinates. As fully detailed in [22], this variational formalism identifies the covariant central force decomposition (cCFD)

$$\mathbf{f}_{\text{cCFD}}^{\alpha\beta} = \sum_{I=1}^M (\nabla_{\mathcal{S}_I} \tilde{V}_I)_{\alpha\beta} \frac{\mathbf{r}^{\alpha\beta}}{r^{\alpha\beta}}, \quad (7)$$

where $\nabla_{\mathcal{S}_I} \tilde{V}_I$ is the covariant derivative of the potential along the shape space \mathcal{S}_I . For four- or fewer-body potentials, cCFD and CFD in Eq. (5) coincide. However, cCFD circumvents the main limitation of CFD by providing a unique expression for potentials with any number of particles. In practice, $(\nabla_{\mathcal{S}_I} \tilde{V}_I)_{\alpha\beta}$ can be computed by projecting $\partial \tilde{V}_I / \partial r^{\alpha\beta}$ for an arbitrary extension onto \mathcal{S}_I [23]. Through a different rationale, the projection of the CFD onto the shape space has been recently discussed in [51]. Our assumption that the potential is additively decomposed into a many-body expansion is appropriate for most classical force fields. For semiempirical methods based on density functional theory concepts, such as the embedded-atom model [20], this additive structure is not apparent. We refer the interested reader to [22,51] for further discussion.

We test the cCFD microscopic stress by considering a coiled-coil structural protein, composed of two identical α -helical chains that wrap around each other to form a superhelix. The coiled-coil structure is a double “zipper,” with an inner core of intercalating hydrophobic amino acids that are flanked by opposing negatively and positively charged amino acids, Fig. 3(a). We model this system as an infinitely long periodic molecule with a widely used protein force field (CHARMM22/CMAP) [21,52] involving up to five-body interactions. We compare the tractions on the surface of the

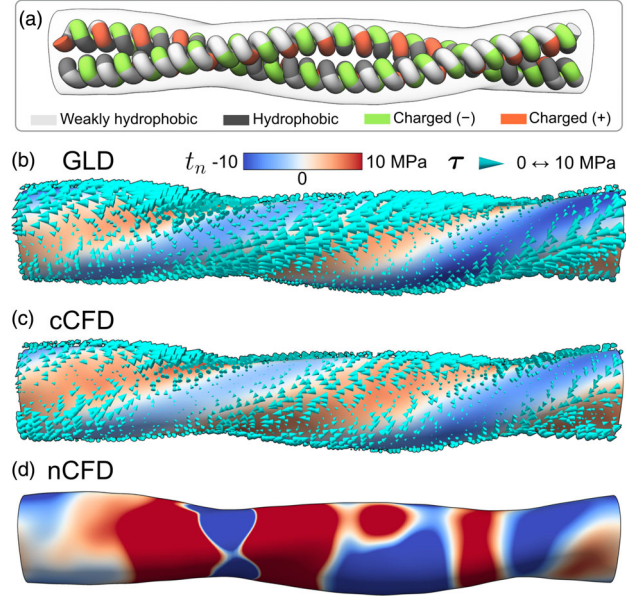


FIG. 3 (color online). The IK stress for force fields beyond four-body interactions. (a) Ribbon representation of a structural coiled-coil protein simulated with the five-body CMAP potential (cross-term energy correction map for adjacent dihedrals used with the CHARMM22 force field). Traction at the surface of the protein are calculated with different variants of the IK stress: GLD (b), cCFD (c), and nCFD (d, see text).

coiled-coil protein, essentially exerted by the solvent, calculated with GLD, cCFD, and another seemingly reasonable way to fix the indeterminacy of CFD (by minimizing the norm of the force decomposition) that we call nCFD [23]. We find that for GLD and cCFD, t_n exhibits a similar pattern that follows the left-handed helical structure, Figs. 3(b) and 3(c). The zippered interface between the two chains is dominated by outward tractions (red), which transition to inward tractions (blue) at the periphery of the protein. In contrast, nCFD produces spurious maps of t_n [Fig. 3(d)], highlighting the need for a physically meaningful method to fix the gauge freedom of CFD [40]. Focusing on τ , cCFD presents tractions that locally equilibrate and do not produce net forces. GLD, however, produces a predominantly leftward traction field following the twist of the protein as a result of the non-symmetric components of σ . Quantitatively, the GLD tractions produce a net force per unit protein length along its axis of 34 mN/m, whereas for cCFD we have 0.35 mN/m. Thus, the GLD stress again contains information about chirality but produces tractions that cannot be physically balanced in our periodic system, which does not undergo any translation or rotation during the course of the simulation.

In summary, the ambiguity of the microscopic stress acutely emerges when analyzing complex materials and biomolecular assemblies. Strikingly, the widely used atomic virial stress does not satisfy balance of linear momentum, while a popular version of the Irving-Kirkwood stress does not satisfy balance of angular momentum as a result of molecular chirality. In contrast, Irving-Kirkwood stress fields based on a covariant central force decomposition can be

rationally derived irrespective of the many-body nature of the potential and satisfy by construction mechanical equilibrium in Eq. (1). This definition of microscopic stress thus provides a solid footing to systematically connect MD simulations and the mechanical behavior of materials at the nanoscale [6,53].

We acknowledge the support of the European Research Council under the European Community's seventh Framework Programme (FP7/2007-2013)/ERC Grant No. 240487, and the computer resources, technical expertise, and assistance provided by the Red Española de Supercomputación. A. T.-S. acknowledges the support of the Spanish government through Grant No. BES-2012-054895. We thank Dr. Bogdan Costescu for assistance with the graphene force field parameters.

A. T.-S. and J. M. V. contributed equally to this work.

*Present address: Center for Biological and Material Sciences, Sandia National Laboratories, Albuquerque, New Mexico, USA.

†marino.arroyo@upc.edu

- [1] J. Li, K. J. Van Vliet, T. Zhu, S. Yip, and S. Suresh, *Nature (London)* **418**, 307 (2002).
- [2] C.-W. Pao, S. M. Foiles, E. B. Webb, D. J. Srolovitz, and J. A. Floro, *Phys. Rev. B* **79**, 224113 (2009).
- [3] Y. Wei, J. Wu, H. Yin, X. Shi, R. Yang, and M. Dresselhaus, *Nat. Mater.* **11**, 759 (2012).
- [4] Z. Song, V. I. Artyukhov, B. I. Yakobson, and Z. Xu, *ACS Nano* **9**, 401 (2015).
- [5] E. Lindahl and O. Edholm, *J. Chem. Phys.* **113**, 3882 (2000).
- [6] M. Hu, D. H. de Jong, S. J. Marrink, and M. Deserno, *Faraday Discuss.* **161**, 365 (2013).
- [7] J. M. Vanegas, A. Torres-Sánchez, and M. Arroyo, *J. Chem. Theory Comput.* **10**, 691 (2014).
- [8] O. H. S. Ollila, H. J. Risselada, M. Louhivuori, E. Lindahl, I. Vattulainen, and S. J. Marrink, *Phys. Rev. Lett.* **102**, 078101 (2009).
- [9] J. M. Vanegas and M. Arroyo, *PLoS One* **9**, e113947 (2014).
- [10] H. W. Hatch and P. G. Debenedetti, *J. Chem. Phys.* **137**, 035103 (2012).
- [11] D. H. Tsai, *J. Chem. Phys.* **70**, 1375 (1979).
- [12] P. Schofield and J. Henderson, *Proc. R. Soc. A* **379**, 231 (1982).
- [13] E. B. Tadmor and R. E. Miller, *Modeling Materials: Continuum, Atomistic and Multiscale Techniques* (Cambridge University Press, Cambridge, England, 2011).
- [14] A. P. Thompson, S. J. Plimpton, and W. Mattson, *J. Chem. Phys.* **131**, 154107 (2009).
- [15] R. Goetz and R. Lipowsky, *J. Chem. Phys.* **108**, 7397 (1998).
- [16] N. C. Admal and E. B. Tadmor, *J. Elast.* **100**, 63 (2010).
- [17] N. C. Admal and E. B. Tadmor, *J. Chem. Phys.* **134**, 184106 (2011).
- [18] H. Heinz, W. Paul, and K. Binder, *Phys. Rev. E* **72**, 066704 (2005).
- [19] H. Heinz, *Mol. Simul.* **33**, 747 (2007).
- [20] M. S. Daw and M. I. Baskes, *Phys. Rev. B* **29**, 6443 (1984).
- [21] A. D. Mackerell, M. Feig, and C. L. Brooks, *J. Comput. Chem.* **25**, 1400 (2004).
- [22] A. Torres-Sánchez, J. M. Vanegas, and M. Arroyo (to be published).
- [23] See Supplemental Material at <http://link.aps.org/supplemental/10.1103/PhysRevLett.114.258102> for extended theory, figures, and information about simulation settings, which includes Refs. [24–33].
- [24] B. Hess, C. Kutzner, D. van Der Spoel, and E. Lindahl, *J. Chem. Theory Comput.* **4**, 435 (2008).
- [25] S. Pronk, S. Páll, R. Schulz, P. Larsson, P. Bjelkmar, R. Apostolov, M. R. Shirts, J. C. Smith, P. M. Kasson, D. van Spoel, B. Hess, and E. Lindahl, *Bioinformatics* **29**, 845 (2013).
- [26] O. Berger, O. Edholm, and F. Jähnig, *Biophys. J.* **72**, 2002 (1997).
- [27] D. P. Tieleman, Structures and topologies for biomembranes and membrane-protein systems, <http://wcm.ucalgary.ca/tieleman/downloads>.
- [28] H. J. C. Berendsen, J. P. M. Postma, and W. F. van Gunsteren, in *Intermolecular Forces*, edited by B. Pullman (Reidel, Dordrecht, 1981), pp. 331–342.
- [29] G. Grigoryan, Coiled-coil crick parameterization, <http://www.grigoryanlab.org/cccp/index.gen.html>.
- [30] G. Grigoryan and W. F. DeGrado, *J. Mol. Biol.* **405**, 1079 (2011).
- [31] E. F. Pettersen, T. D. Goddard, C. C. Huang, G. S. Couch, D. M. Greenblatt, E. C. Meng, and T. E. Ferrin, *J. Comput. Chem.* **25**, 1605 (2004).
- [32] J. Y. Su, R. S. Hodges, and C. M. Kay, *Biochemistry* **33**, 15501 (1994).
- [33] W. L. Jorgensen, J. Chandrasekhar, J. D. Madura, R. W. Impey, and M. L. Klein, *J. Chem. Phys.* **79**, 926 (1983).
- [34] J. H. Irving and J. G. Kirkwood, *J. Chem. Phys.* **18**, 817 (1950).
- [35] W. Noll, *Indiana Univ. Math. J.* **4**, 627 (1955).
- [36] B. I. Costescu, I. B. Baldus, and F. Gräter, *Phys. Chem. Chem. Phys.* **16**, 12591 (2014).
- [37] J. M. Vanegas, A. Torres-Sánchez, and M. Arroyo, Computing the local stress tensor in classical MD simulations, <http://www.lacan.upc.edu/LocalStressFromMD>.
- [38] A. I. Murdoch, *J. Elast.* **71**, 105 (2003).
- [39] H. Wagner, *J. Stat. Phys.* **55**, 1293 (1989).
- [40] A. I. Murdoch, *Physical Foundations of Continuum Mechanics*, 1st ed. (Cambridge University Press, Cambridge, England, 2012).
- [41] B. Seguin and E. Fried, *Arch. Ration. Mech. Anal.* **206**, 1039 (2012).
- [42] D. Marsh, *Chem. Phys. Lipids* **144**, 146 (2006).
- [43] W. Helfrich, *J. Phys. Condens. Matter* **6**, A79 (1994).
- [44] R. G. Littlejohn and M. Reinsch, *Rev. Mod. Phys.* **69**, 213 (1997).
- [45] J. Porta, L. Ros, F. Thomas, and C. Torras, *IEEE. Trans. Robot.* **21**, 176 (2005).
- [46] L. Mistura, *Int. J. Thermophys.* **8**, 397 (1987).
- [47] M. Baus and R. Lovett, *Phys. Rev. Lett.* **65**, 1781 (1990).
- [48] G. C. Rossi and M. Testa, *J. Chem. Phys.* **132**, 074902 (2010).
- [49] T. Doyle and J. Ericksen, in *Advances in Applied Mechanics IV*, edited by H. L. Dryden and Th. von Kármán (Elsevier, New York, 1956), Vol. 4, pp. 53–115.
- [50] J. Marsden and T. J. R. Hughes, *Mathematical Foundations of Elasticity* (Dover Publications, Inc., New York, 1983).
- [51] N. C. Admal, Ph.D. thesis, University of Minnesota, 2014.
- [52] A. MacKerell and D. Bashford, *J. Phys. Chem. B* **102**, 3586 (1998).
- [53] Z. Zhang, X. Wang, and J. D. Lee, *J. Appl. Phys.* **115**, 114314 (2014).

SUPPLEMENTAL MATERIAL

Examining the mechanical equilibrium of microscopic stresses in molecular simulations

Alejandro Torres-Sánchez¹, Juan M. Vanegas^{1,2} and Marino Arroyo^{1,*}

[1] Laboratori de Càlcul Numèric, Universitat Politècnica de Catalunya-BarcelonaTech, Barcelona, Spain

[2] Current Address: Center for Biological and Material Sciences, Sandia National Laboratories, Albuquerque, New Mexico

* marino.arroyo@upc.edu

Supplemental Material

1	Supplemental figures	2
2	Theory	7
2.1	Irving-Kirkwood framework: conservation of linear momentum and force decompositions	7
2.2	Conservation of angular momentum: Central Force Decomposition and Covariant Central Force Decomposition	8
2.3	Numerical implementation	9
2.4	Stress smoothing and calculation of its divergence	12
3	Simulation methods and analysis	13
3.1	Local stress calculations	13
3.2	Graphene	13
3.3	DPPC bilayer	13
3.4	Coiled-coil	14

1 Supplemental figures

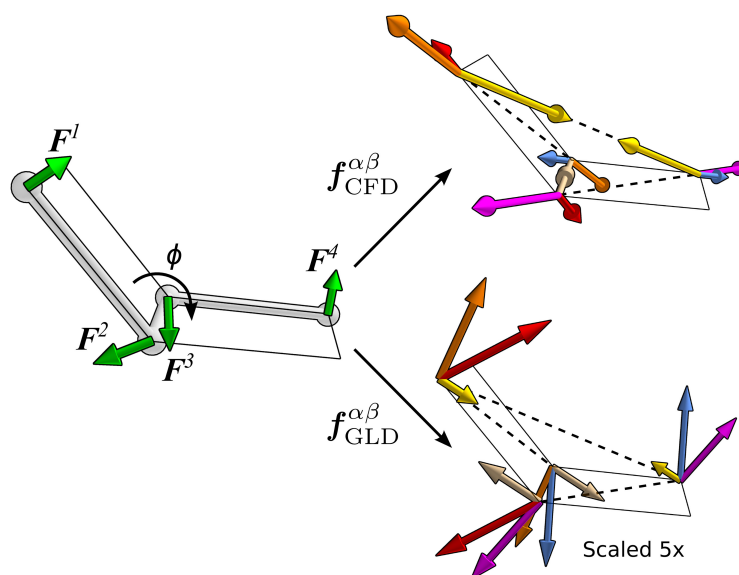


Figure 1: **Pairwise forces obtained from different decompositions.** Torsional potential acting on four atoms as determined by a dihedral angle ϕ (left). Net forces on each atom are displayed in green. The resulting decomposed forces in the case of CFD (top) and GLD (bottom, scaled 5x for visualization purposes) are shown on the right. There is a great difference both in the magnitude and direction of the resulting force pairs. While the CFD forces are always central (i.e. parallel to $r^{\alpha\beta}$), the GLD pairs are not central, and much smaller than those of CFD.

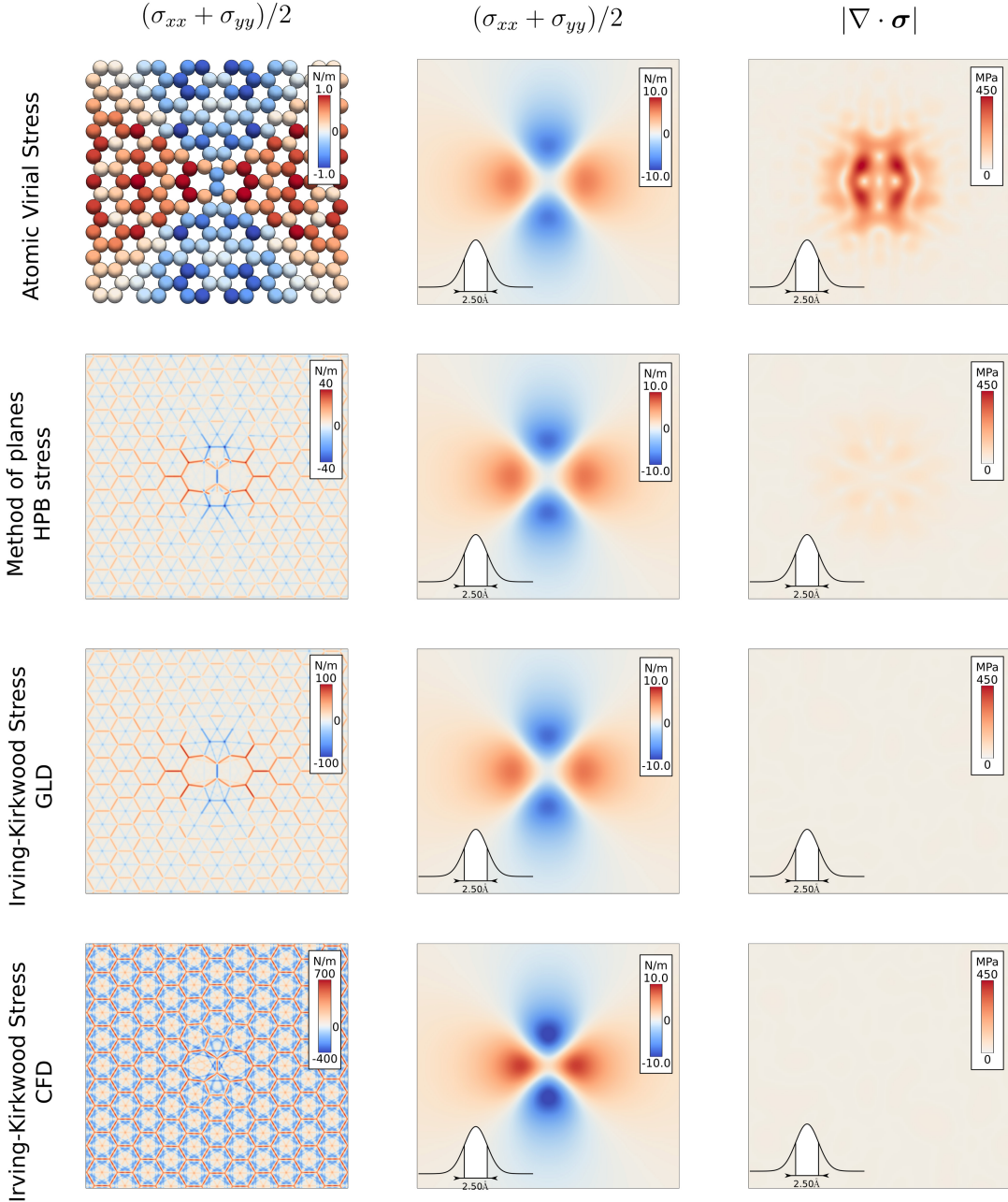


Figure 2: **The atomic virial stress and the method of planes of Heinz-Paul-Binder (HPB) [18, 19] violate conservation of linear momentum.** The left column shows the raw stress fields for each stress definition. The HPB stress produces fields similar to those of IK-GLD, with stresses concentrated along interaction lines. However, the interaction lines of the former join the positions of geometric centers, which sometimes do not coincide with the positions of the atoms, whereas the interaction lines of the latter always join atomic positions, as for the IK-CFD definition. Due to the decomposition, see Fig. S1, the dihedral interaction lines present large stresses for the IK-CFD while these are much smaller for the IK-GLD definition. The middle column shows the smoothed stress fields, where we appreciate that the HPB stress and the IK-GLD stress are very similar to the IK-CFD stress, but with slightly smaller magnitudes. The right column shows the divergence of each stress field. While the IK-CFD and the IK-GLD stresses are divergence-free, and thus self-equilibrated, the HPB stress is out-of-equilibrium, yet with a smaller force density than that of the atomic virial definition.

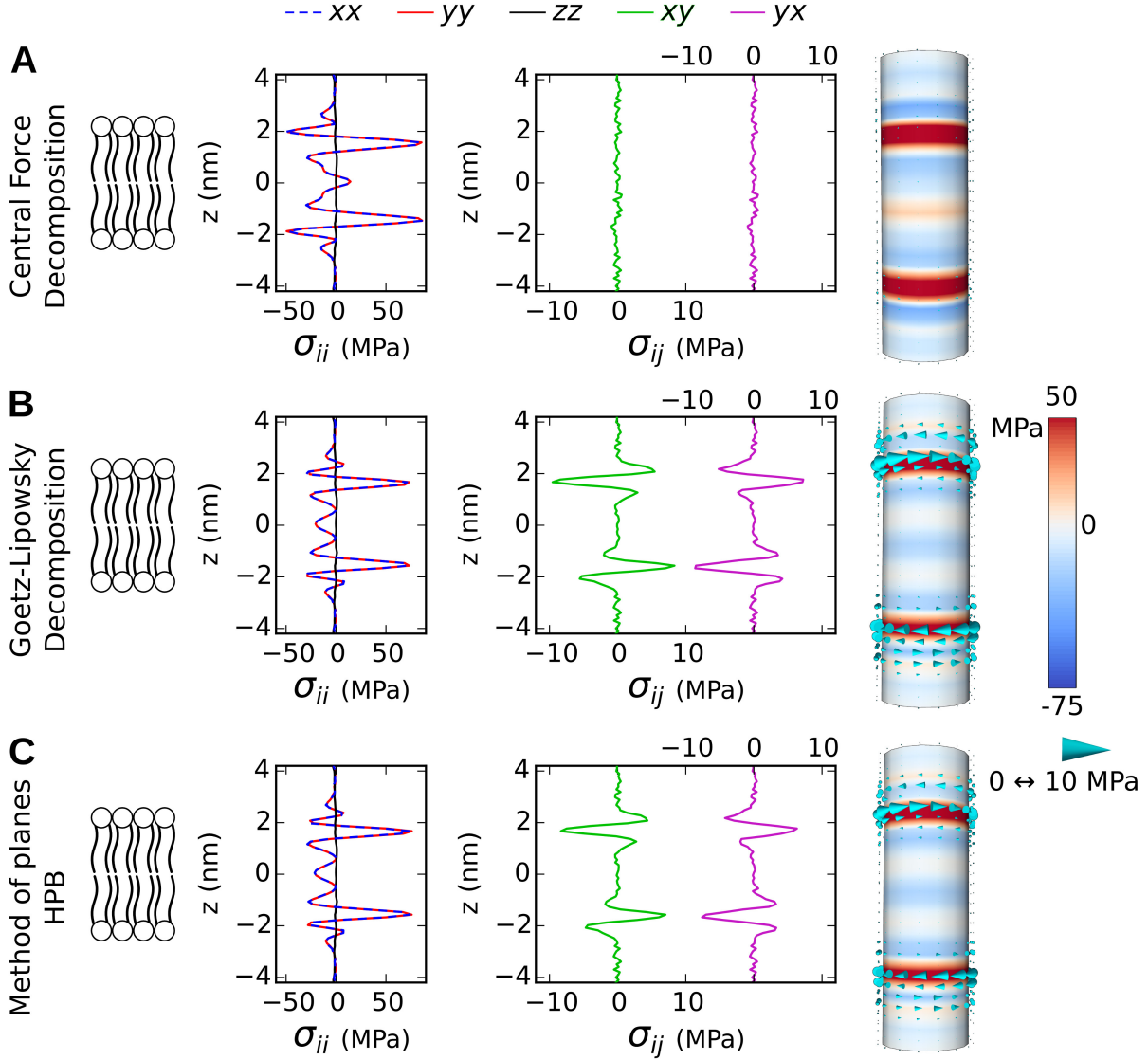


Figure 3: **IK-GLD and the HPB stress [18, 19] violate conservation of angular momentum in a DPPC bilayer.** (A) IK-CFD stress profiles for the DPPC bilayer. Due to the fluidity of the bilayer, the IK-CFD stress is diagonal for this system. (B) IK-GLD stress profiles. In this case, the violation of the conservation of angular momentum is clear from the presence of antisymmetric off-diagonal components that create torque densities in the membrane. (C) The HPB stress behaves similarly to the IK-GLD stress, violating conservation of angular momentum, yet with somewhat smaller torques. For all three stress definitions, we observe that $\sigma_{yy} = \sigma_{xx}$, $\sigma_{zz}(z) = \text{cst}$, and $\sigma_{\cdot z} = \sigma_z = 0$ ($\cdot = x, y$) within numerical error.

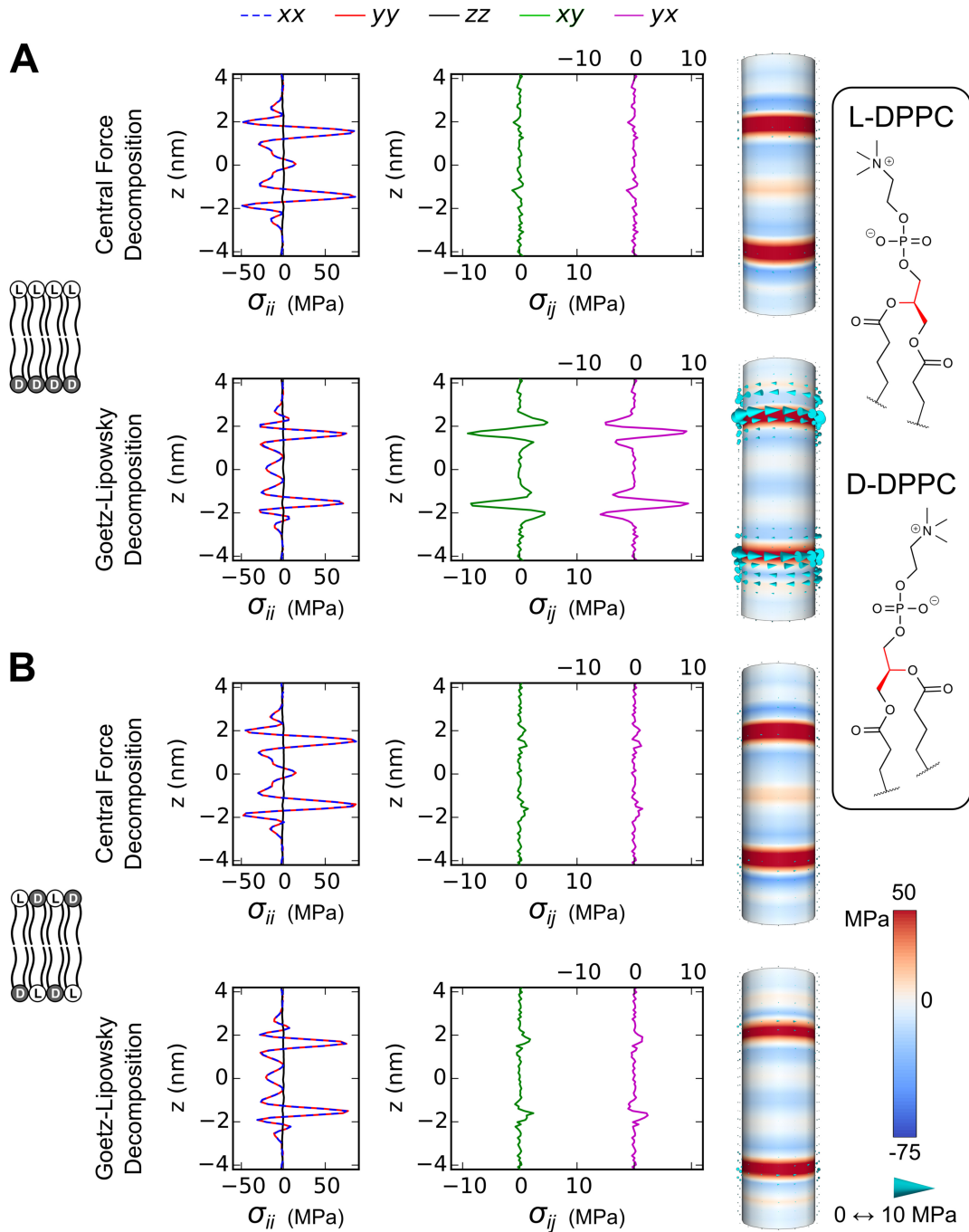


Figure 4: **Effect of chirality in the IK-CFD stress and IK-GLD stress.** (A) IK-CFD and IK-GLD stresses for a bilayer composed of a monolayer of L-DPPC lipids and a monolayer of D-DPPC lipids (see inset on the left). While the IK-CFD stress is diagonal, the IK-GLD off-diagonal stress profiles are opposite to those in the membrane composed of two monolayers of L-DPPC lipids for the lower monolayer (see Fig. S3). (B) IK-CFD and IK-GLD stresses for a bilayer composed of a two monolayer with homogeneous mixture of L-DPPC lipids and D-DPPC lipids. The IK-CFD stress remains diagonal regardless of the chirality of the lipids. In B, the IK-GLD stress is also diagonal. From all these calculations we conclude that the torque densities generated in the IK-GLD stresses stem from the internal chirality of the lipids. The HPB stress presents a similar behavior to that of the IK-GLD stress (data not shown).

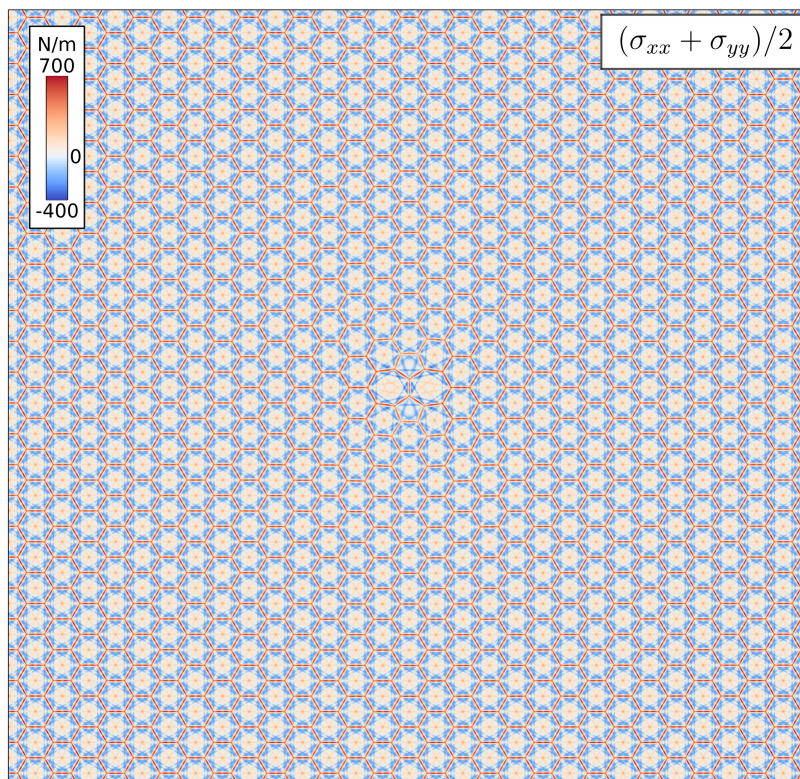


Figure 5: **Our microscopic stress calculation is consistent with periodic boundary conditions.** Trace of the IK-CFD stress tensor over the whole computational domain for the defective graphene system. No spurious stress distributions are present near the boundaries of the computational box.

2 Theory

2.1 Irving-Kirkwood framework: conservation of linear momentum and force decompositions

In the Irving-Kirkwood framework, the continuum density field is defined as

$$\rho(\mathbf{x}) = \sum_{\alpha=1}^N \langle m^\alpha \delta(\mathbf{r}^\alpha - \mathbf{x}) \rangle, \quad (1)$$

where $\langle \cdot \rangle$ stands for an ensemble average, m^α and \mathbf{r}^α are the mass and position of particle α , $\delta(\mathbf{x})$ is the 3D Dirac distribution centered at $\mathbf{0}$, and N is the total number of particles in the system. Invoking the equivalence of the macroscopic momentum $\rho(\mathbf{x})\mathbf{v}(\mathbf{x})$ and the microscopic momentum $\sum_{\alpha}^N \langle m^\alpha \mathbf{v}^\alpha \delta(\mathbf{r}^\alpha - \mathbf{x}) \rangle$, the continuum velocity field is defined as

$$\mathbf{v}(\mathbf{x}) = \frac{1}{\rho(\mathbf{x})} \sum_{\alpha=1}^N \langle m^\alpha \mathbf{v}^\alpha \delta(\mathbf{r}^\alpha - \mathbf{x}) \rangle, \quad (2)$$

where \mathbf{v}^α is the velocity of particle α . These two fields satisfy the continuity equation $\partial\rho/\partial t + \rho\nabla \cdot \mathbf{v} = 0$, expressing balance of mass in continuum mechanics, where $\nabla \cdot$ stands for the divergence operator. In the absence of external forces, the continuum balance of linear momentum requires that

$$\nabla \cdot \boldsymbol{\sigma}(\mathbf{x}) = \rho(\mathbf{x}) \frac{d\mathbf{v}(\mathbf{x})}{dt}. \quad (3)$$

After invoking Liouville's equation, one finds that [16, 13]

$$\begin{aligned} \nabla \cdot \boldsymbol{\sigma}(\mathbf{x}) = & \nabla \cdot \left(\sum_{\alpha=1}^N \langle m^\alpha \mathbf{v}^\alpha \otimes \mathbf{v}^\alpha \delta(\mathbf{r}^\alpha - \mathbf{x}) \rangle \right) - \\ & - \sum_{\alpha=1}^N \langle \mathbf{F}^\alpha \delta(\mathbf{r}^\alpha - \mathbf{x}) \rangle, \end{aligned} \quad (4)$$

where \mathbf{F}^α is the force on particle α and $\mathbf{a} \otimes \mathbf{b}$ denotes the dyadic product of vectors \mathbf{a} and \mathbf{b} .

If Eq. (4) is used to derive an expression for $\boldsymbol{\sigma}$, this definition is clearly non-unique since given any stress $\boldsymbol{\sigma}$ satisfying Eq. (4), we can add any divergence-free field $\boldsymbol{\omega}$ to $\boldsymbol{\sigma}$ with the resulting field $\boldsymbol{\sigma} + \boldsymbol{\omega}$ also satisfying this equation. An expression of $\boldsymbol{\sigma}$ that satisfies Eq. (4) by construction is [34, 35]

$$\begin{aligned} \boldsymbol{\sigma}(\mathbf{x}) &= \boldsymbol{\sigma}_K(\mathbf{x}) + \boldsymbol{\sigma}_V(\mathbf{x}), \\ \boldsymbol{\sigma}_K(\mathbf{x}) &= - \left\langle \sum_{\alpha} m^\alpha \mathbf{v}^\alpha \otimes \mathbf{v}^\alpha \delta(\mathbf{r}^\alpha - \mathbf{x}) \right\rangle, \\ \boldsymbol{\sigma}_V(\mathbf{x}) &= \left\langle \sum_{\alpha, \beta > \alpha} \mathbf{f}^{\alpha\beta} \otimes \mathbf{r}^{\alpha\beta} B(\mathbf{r}^\alpha, \mathbf{r}^\beta; \mathbf{x}) \right\rangle, \end{aligned} \quad (5)$$

where $\mathbf{r}^{\alpha\beta} = \mathbf{r}^\beta - \mathbf{r}^\alpha$, $\mathbf{f}^{\alpha\beta}$ are the terms of a force decomposition, $\mathbf{F}^\alpha = \sum_{\beta=1}^N \mathbf{f}^{\alpha\beta}$ satisfying $\mathbf{f}^{\alpha\beta} = -\mathbf{f}^{\beta\alpha}$, and $B(\mathbf{r}^\alpha, \mathbf{r}^\beta; \mathbf{x}) = \int_0^1 \delta[(1-s)\mathbf{r}^\alpha + s\mathbf{r}^\beta - \mathbf{x}] ds$ is the bond function that spreads

to contribution from the pair $\alpha\beta$ to the stress along the line segment joining the particles [35]. The lack of uniqueness in the definition of the stress is present in this formulation since the force decomposition is not unique. For instance, let the potential of the system be described additively as $V = \sum_{I=1}^M V_I$, with each contribution involving n_I particles, then the Goetz-Lipowsky force decomposition is [15]

$$\mathbf{f}_{\text{GLD}}^{\alpha\beta} = \sum_{I=1}^M \frac{1}{n_I} \left(\frac{\partial V_I}{\partial \mathbf{r}^\beta} - \frac{\partial V_I}{\partial \mathbf{r}^\alpha} \right). \quad (6)$$

This decomposition satisfies the requirement that $\mathbf{f}^{\alpha\beta} = -\mathbf{f}^{\beta\alpha}$. However, as shown in the experiments performed in this work, the IK-GLD is not symmetric, which therefore violates conservation of angular momentum for simple bodies.

2.2 Conservation of angular momentum: Central Force Decomposition and Covariant Central Force Decomposition

Conservation of angular momentum in a continuum theory of simple bodies in the absence of external torque densities requires the stress to be symmetric, i.e. $\sigma_{ij} = \sigma_{ji}$. Not all force decompositions compatible with conservation of linear momentum, i.e. $\mathbf{f}^{\alpha\beta} = -\mathbf{f}^{\beta\alpha}$, lead to conservation of angular momentum in the IK setting. It has been recently shown [16] that the central force decomposition (CFD) is the only possible choice to obtain a symmetric stress by construction. To define this decomposition, let us express the classical potential as a sum of many-body contributions, $V = \sum_{I=1}^M V_I$, where V_I involves n_I particles and cannot be described as a sum of lower-body interactions. Then, the CFD decomposition follows from

$$\mathbf{f}_{\text{CFD}}^{\alpha\beta} = \sum_{I=1}^M \frac{\partial \tilde{V}_I}{\partial r^{\alpha\beta}} \frac{\mathbf{r}^{\alpha\beta}}{r^{\alpha\beta}}, \quad (7)$$

where \tilde{V}_I is a representation of the interatomic potential in terms of particle distances $r^{\alpha\beta} = |\mathbf{r}^{\alpha\beta}|$. Such a representation always exists as result of the invariance with respect to rigid body transformations of classical potentials [13].

However, CFD has an important limitation when $n_I > 4$. To show this, we first note that the $n_I(n_I + 1)/2$ interatomic distances $(r^{12}, \dots, r^{(n_I-1)n_I})$ involved in a given multibody potential V_I cannot be arbitrarily chosen in $\mathcal{D}_I = \mathbb{R}_+^{n_I(n_I+1)/2}$. There are geometric conditions that guarantee that these distances can be realized by a system of n_I particles, which define the so-called shape space $\mathcal{S}_I \subset \mathcal{D}_I$. These geometric conditions are expressed in terms of Caley-Menger determinants. More precisely, the sets of distances need to satisfy [13, 44, 45]

$$\begin{aligned} \chi(r^{\alpha\beta}, r^{\alpha\gamma}, r^{\beta\gamma}) &\leq 0 \\ \chi(r^{\alpha\beta}, r^{\alpha\gamma}, r^{\alpha\delta}, \dots, r^{\gamma\delta}) &\leq 0 \\ \chi(r^{\alpha\beta}, r^{\alpha\gamma}, r^{\alpha\delta}, r^{\alpha\epsilon}, \dots, r^{\delta\epsilon}) &= 0 \\ \chi(r^{\alpha\beta}, r^{\alpha\gamma}, r^{\alpha\delta}, r^{\alpha\epsilon}, r^{\alpha\zeta}, \dots, r^{\epsilon\zeta}) &= 0 \end{aligned} \quad (8)$$

where $\chi(r^{12}, \dots, r^{(N-1), N})$ is the Caley-Menger determinant given by

$$\chi(r^{12}, \dots, r^{(N-1), N}) = \det \begin{pmatrix} 0 & s^{12} & s^{13} & \dots & s^{1N-1} & s^{1N} & 1 \\ s^{12} & 0 & s^{23} & \dots & s^{2N-1} & s^{2N} & 1 \\ s^{13} & s^{23} & 0 & \dots & s^{3N-1} & s^{3N} & 1 \\ \vdots & \vdots & \vdots & \ddots & \vdots & \vdots & \vdots \\ s^{1N-1} & s^{2N-1} & s^{3N-1} & \dots & 0 & s^{N-1, N} & 1 \\ s^{1N} & s^{2N} & s^{3N} & \dots & s^{N-1, N} & 0 & 1 \\ 1 & 1 & 1 & 1 & 1 & 1 & 0 \end{pmatrix} = 0, \quad (9)$$

where $s^{\alpha\beta} = (r^{\alpha\beta})^2$. The first 2 equations in Eq. (8) are inequalities involving 3 and 4 particles respectively and restrict \mathcal{S}_I to a part of \mathcal{D}_I , but do not modify the intrinsic dimension of \mathcal{S}_I . Therefore, for potentials involving up to 4-body interactions, the differential calculus in Eq. (7) can be directly applied. However, the last two equations in Eq. (8), which involve 5 and 6 particles respectively, restrict the intrinsic dimension of \mathcal{S}_I . Therefore, when $n_I > 4$, the dimension of the manifold \mathcal{S}_I is smaller than $n_I(n_I + 1)/2$, and therefore the differential calculus involved in Eq. (7) needs to be carefully considered [44, 45]. Noting this fact, it has been argued that, to be able to take the partial derivative $\partial \tilde{V}_I / \partial r^{\alpha\beta}$ in Eq. (7), the potential needs to be extended to \mathcal{D}_I [16, 13]. However, when $n_I > 4$, there exists infinitely many extensions, leading to an extension-dependent force decomposition and an ambiguous definition of the stress, all of which differ by divergence-free fields. The lack of a rational procedure to fix this gauge freedom has been a source of criticism [40].

Following an alternative yet compatible path to the IK derivation of the stress based on covariance arguments (see main text), we propose an unambiguous CFD [22]. This central force decomposition, which we call covariant central force decomposition (cCFD), can be computed by just replacing the partial derivatives in Eq. (7) by covariant derivatives along \mathcal{S}_I ,

$$\mathbf{f}_{\text{cCFD}}^{\alpha\beta} = \sum_{I=1}^M \left[\nabla_{\mathcal{S}_I} \tilde{V}_I \right]_{\alpha\beta} \frac{\mathbf{r}^{\alpha\beta}}{r^{\alpha\beta}}, \quad (10)$$

This procedure leads to a uniquely defined CFD regardless of the extension that is used to compute the stress and completely fixes the Gauge invariance in the IK stress, since the covariant derivative of the potential is uniquely defined. This definition is based on the assumption that the potential V is written as a sum $\sum_I V_I$ of n -body potentials V_I that cannot be written in terms of lower-body interactions (i.e. cannot be further reduced). In biomolecular simulations, these potentials are 2-, 3-, 4- and 5-body (Coulomb, van der Waals, angles, dihedrals and CMAP) interactions. For a discussion about the treatment of more general force fields, see [51, 22]. A numerical procedure to compute the cCFD for 5 and higher-body potentials is proposed in the next section.

2.3 Numerical implementation

In our algorithm to compute the local stress, we read velocities and forces from GROMACS 4.5.5 as explained in reference [7] and in the manual of our implementation [37]. Thus, for each frame, we receive $\{\mathbf{v}^\alpha\}_{\alpha=1, \dots, N}$ and $\{\mathbf{F}_I^\alpha = -\partial V_I^\alpha / \partial \mathbf{r}^\alpha\}_{\alpha=1, \dots, N}$ for each potential V_I in the force field, $V = \sum_I V_I$.

Assuming this as an input, the kinetic part of the stress can be easily calculated and spread into the grid (we refer to [7] for a detailed explanation of the spreading process). For GLD, we compute pairwise terms following Eq. (6) and spread each contribution into the grid. For the HPB stress, we follow the prescriptions in [18, 19]. The computation of the decompositions CFD, cCFD is detailed next.

Consider a potential V_I with $n_I = N$ interacting particles. The set of forces $\mathbf{F}^1, \dots, \mathbf{F}^N$ is an input. We want to find the set of pairwise forces $\varphi^{\alpha\beta} \hat{\mathbf{r}}^{\alpha\beta}$, where $\hat{\mathbf{r}}^{\alpha\beta} = \mathbf{r}^{\alpha\beta} / r^{\alpha\beta}$, satisfying

$$\sum_{\beta} \varphi^{\alpha\beta} \hat{\mathbf{r}}^{\alpha\beta} = \mathbf{F}^{\alpha}, \quad \forall \alpha. \quad (11)$$

Introducing the notation $\hat{\mathbf{r}}^{\alpha\beta} = (\hat{x}^{\alpha\beta}, \hat{y}^{\alpha\beta}, \hat{z}^{\alpha\beta})$, we can write these relations in matrix form as

$$\underbrace{\begin{pmatrix} \hat{x}^{12} & \dots & \hat{x}^{1N} & 0 & \dots & 0 & \dots & 0 \\ \hat{y}^{12} & \dots & \hat{y}^{1N} & 0 & \dots & 0 & \dots & 0 \\ \hat{z}^{12} & \dots & \hat{z}^{1N} & 0 & \dots & 0 & \dots & 0 \\ -\hat{x}^{12} & \dots & 0 & \hat{x}^{23} & \dots & \hat{x}^{2N} & \dots & 0 \\ -\hat{y}^{12} & \dots & 0 & \hat{y}^{23} & \dots & \hat{y}^{2N} & \dots & 0 \\ -\hat{z}^{12} & \dots & 0 & \hat{z}^{23} & \dots & \hat{z}^{2N} & \dots & 0 \\ \vdots & \ddots & \vdots & \vdots & \ddots & \vdots & \ddots & \vdots \\ 0 & \dots & -\hat{z}^{1N} & 0 & \dots & -\hat{z}^{2N} & \dots & \hat{z}^{(N-1),N} \end{pmatrix}}_{\mathbf{D}, \dim = m \times n} \underbrace{\begin{pmatrix} \varphi_{12} \\ \vdots \\ \varphi_{1N} \\ \varphi_{23} \\ \vdots \\ \varphi_{2N} \\ \vdots \\ \varphi_{(N-1),N} \end{pmatrix}}_{\boldsymbol{\varphi}, \dim = n} = \underbrace{\begin{pmatrix} F_x^1 \\ F_y^1 \\ F_z^1 \\ F_x^2 \\ F_y^2 \\ F_z^2 \\ \vdots \\ F_z^N \end{pmatrix}}_{\mathbf{F}, \dim = m}, \quad (12)$$

where $m = 3N$, $n = N(N-1)/2$ and the rank of this system is $r = 3N - 6$ (number of independent equations). For systems with $N = 3, 4$, this system has a unique solution. However, for $N > 4$ this system is underdetermined.

To obtain a particular solution to Eq. (12) we resort to the DGELSD function of the LAPACK library. This function computes the solution $\boldsymbol{\varphi}$ with minimum norm amongst all solutions of Eq. (12). This leads to the results of nCFD for the coiled-coil shown in the main text. To obtain the cCFD, we use this nCFD as a seed and apply the method explained next.

The covariant derivative in Eq. (10) can be computed from the partial derivative in Eq. (7) for any extension of \tilde{V}_I to \mathcal{D}_I followed by a projection onto \mathcal{S}_I . In practical terms, given a set of atomic forces $\{\mathbf{F}^{\alpha}\}_{\alpha=1,\dots,N}$ this means that after obtaining a particular solution of $\boldsymbol{\varphi}$, $\varphi_{\alpha\beta} = \partial \tilde{V} / \partial r^{\alpha\beta}$, from Eq. (12), we need to project the result onto \mathcal{S}_I to obtain $\boldsymbol{\varphi}_{\mathcal{S}_I}$, whose components are precisely $\left(\nabla_{\mathcal{S}_I} \tilde{V}_I \right)_{\alpha\beta}$. $\boldsymbol{\varphi}_{\mathcal{S}_I}$ is extension-independent as well as independent of the choice of particular solution of Eq. (12). This coincides with the usual definition of the covariant derivative in a manifold that is embedded in Euclidean space. For 3- and 4-body interactions, this projection is the identity.

For the special case of 5-body potentials, such as the CMAP interaction present in our coiled-coil model, the distance space is $\mathcal{D}_I = \mathbb{R}^{10}$ and the shape space, which has dimension 9,

is given by the equation

$$\chi(r^{12}, \dots, r^{45}) = \det \begin{pmatrix} 0 & s^{12} & s^{13} & s^{14} & s^{15} & 1 \\ s^{12} & 0 & s^{23} & s^{24} & s^{25} & 1 \\ s^{13} & s^{23} & 0 & s^{34} & s^{35} & 1 \\ s^{14} & s^{24} & s^{34} & 0 & s^{45} & 1 \\ s^{15} & s^{25} & s^{35} & s^{45} & 0 & 1 \\ 1 & 1 & 1 & 1 & 1 & 0 \end{pmatrix} = 0. \quad (13)$$

Then, taking into account that the (non-unit) normal to \mathcal{S}_I is given by

$$\mathbf{n}_{\mathcal{S}_I} = \begin{pmatrix} \frac{\partial \chi}{\partial r^{12}} \\ \vdots \\ \frac{\partial \chi}{\partial r^{45}} \end{pmatrix}, \quad (14)$$

we have

$$\varphi_{\mathcal{S}_I} = \varphi - \frac{1}{|\mathbf{n}_{\mathcal{S}_I}|^2} \mathbf{n}_{\mathcal{S}_I} \mathbf{n}_{\mathcal{S}_I}^T \varphi \quad (15)$$

Thus, we obtain the cCFD for 5-body potentials from the following procedure:

1. Compute a CFD from the linear system Eq. (12).
2. Compute the gradient of the Cayley-Menger determinant $\chi(r^{12}, \dots, r^{45})$.
3. Project the CFD onto \mathcal{S}_I following (15).

This method is very efficient for 5-body potentials since the gradient of the Cayley-Menger determinant can be evaluated analytically. For higher-body potentials, we propose next an equivalent method based on algebraic arguments. This procedure provides a method to compute the cCFD without an analytic expression for all (possibly non-independent) gradients of the corresponding Cayley-Menger determinants, and therefore is best suited for higher-body interactions.

First, we note that the normal space to the shape space \mathcal{S}_I is precisely the kernel of \mathbf{D} (see Eq. (12)), i.e. it is the vector space spanned by the solutions of

$$\mathbf{D}\mathbf{X} = \mathbf{0}. \quad (16)$$

Any component of the force decomposition on this space does not alter the net forces on the particles, as can be checked by comparing Eqs. (12) and (16). The solution to this problem can be computed through a QR decomposition. Let \mathbf{D}^T be the transpose of \mathbf{D} . Its QR decomposition exists and has the general form

$$\mathbf{D}^T \mathbf{P} = \mathbf{Q}\mathbf{R} = (\mathbf{Q}_1 \quad \mathbf{Q}_2) \begin{pmatrix} \mathbf{R}_1 & \mathbf{R}_2 \\ \mathbf{0} & \mathbf{0} \end{pmatrix} \quad (17)$$

where

- \mathbf{Q} is an orthogonal matrix of dimension $n \times n$.

- \mathbf{Q}_1 is a $n \times r$ with orthonormal columns (this is uniquely defined).
- \mathbf{Q}_2 is a $n \times (n - r)$ with orthonormal columns.
- \mathbf{R}_1 is a $r \times r$ upper triangular and invertible.
- \mathbf{R}_2 is a $r \times (m - r)$ matrix.
- \mathbf{P} is a $m \times m$ pivoting matrix.

Then we can rewrite Eq. (16) as

$$\mathbf{D}\mathbf{X} = \mathbf{P}\mathbf{R}^T\mathbf{Q}^T\mathbf{X} = \mathbf{P} \begin{pmatrix} \mathbf{R}_1^T & \mathbf{0} \\ \mathbf{R}_2^T & \mathbf{0} \end{pmatrix} \begin{pmatrix} \mathbf{Q}_1^T \\ \mathbf{Q}_2^T \end{pmatrix} \mathbf{X} = \mathbf{0}. \quad (18)$$

Taking into account that \mathbf{Q} is an orthogonal matrix, its columns form an orthonormal basis of \mathbb{R}^n . We can then define the two components of \mathbf{X} on the subspaces spanned by the columns of \mathbf{Q}_1 and \mathbf{Q}_2 , $\mathbf{X}_1 = \mathbf{Q}_1^T\mathbf{X}$, $\mathbf{X}_2 = \mathbf{Q}_2^T\mathbf{X}$. Inserting this decomposition in Eq. (18) we obtain the equivalent system

$$\begin{pmatrix} \mathbf{R}_1^T\mathbf{X}_1 \\ \mathbf{R}_2^T\mathbf{X}_1 \end{pmatrix} = \mathbf{0}. \quad (19)$$

Since \mathbf{R}_1^T is invertible, this results in $\mathbf{X}_1 = \mathbf{0}$, while the component \mathbf{X}_2 is completely free. In other words, the kernel of \mathbf{D} is the subspace formed by the column vectors of \mathbf{Q}_2 . Therefore, given a CFD φ , its projection onto the shape space is simply

$$\varphi_{S_I} = \mathbf{Q}_1\mathbf{Q}_1^T\varphi. \quad (20)$$

We resort to the implementation of the QR decomposition in the DGEQRF function of LAPACK.

2.4 Stress smoothing and calculation of its divergence

It is convenient to spatially average the microscopic stress fields with discrete features as

$$\bar{\boldsymbol{\sigma}}(\mathbf{x}) = \int_{\mathbb{R}^3} w(|\mathbf{x} - \mathbf{y}|)\boldsymbol{\sigma}(\mathbf{y})d\mathbf{y}, \quad (21)$$

where $w(r)$ is a normalized compactly-supported weighting function [38, 13]. For the atomic virial stress, this averaging can be applied by interpreting it as a field of concentrated Dirac distributions at the atoms, i.e. $\boldsymbol{\sigma}(\mathbf{x}) = \sum_{\alpha} \delta(\langle \mathbf{r}^{\alpha} - \mathbf{x} \rangle)\boldsymbol{\sigma}^{\alpha}$. The divergence of these spatially averaged stress fields has an important property:

$$\begin{aligned} \bar{\sigma}_{ij,j}(\mathbf{x}) &= \frac{\partial}{\partial x_j} \int_{\mathbb{R}^3} w(|\mathbf{x} - \mathbf{y}|)\sigma_{ij}(\mathbf{y})d\mathbf{y} = \\ &= \int_{\mathbb{R}^3} \frac{\partial w(|\mathbf{x} - \mathbf{y}|)}{\partial x_j} \sigma_{ij}(\mathbf{y})d\mathbf{y} = \\ &= - \int_{\mathbb{R}^3} \frac{\partial w(|\mathbf{x} - \mathbf{y}|)}{\partial y_j} \sigma_{ij}(\mathbf{y})d\mathbf{y} = \\ &= \int_{\mathbb{R}^3} w(|\mathbf{x} - \mathbf{y}|)\sigma_{ij,j}(\mathbf{y})d\mathbf{y} \end{aligned} \quad (22)$$

where we have employed that $\partial w/\partial x_j = -\partial w/\partial y_j$ and integration by parts. This shows that the divergence of the spatially averaged stress is the spatially averaged divergence of the raw stress fields, and thus it must satisfy the same balance equation of the raw divergence, which in the absence of external applied force densities is $\sigma_{ij,j} = 0$ (see the main text). Practically, we compute the divergence from

$$\begin{aligned}\bar{\sigma}_{ij,j}(\mathbf{x}) &= \frac{\partial}{\partial x_j} \int_{\mathbb{R}^3} w(|\mathbf{x} - \mathbf{y}|) \sigma_{ij}(\mathbf{y}) d\mathbf{y} = \\ &= \int_{\mathbb{R}^3} w'(|\mathbf{x} - \mathbf{y}|) \frac{x_j - y_j}{|\mathbf{x} - \mathbf{y}|} \sigma_{ij}(\mathbf{y}) d\mathbf{y}\end{aligned}\tag{23}$$

3 Simulation methods and analysis

All simulations were conducted with the GROMACS 4.5.5 simulation package [24, 25] at the Barcelona Supercomputing Center.

3.1 Local stress calculations

We compute the local stress with our freely available implementation [7, 37]. This implementation, which is based on GROMACS-4.5.5, computes the stress for the different definitions in this article: atomic virial, HPB stress (we have implemented the HPB method of planes as outlined in [19, 18]), IK-GLD, IK-nCFD and IK-cCFD, using a discretization in a 3D grid. For the discretization we employ trilinear weighting functions, which lead to good compromise between both smoothing and preserving the locality of the microscopic stress. Periodic boundary conditions are handled by considering always the closest periodic image of two interacting particles, see Fig. 5. This implementation also deals with constraints in a consistent manner, as explained in [7].

3.2 Graphene

The graphene sheet with the Stone-Wales defect was simulated with a Morse-potential modified version of the OPLS-AA FF [36] for 500 ns of data collection where the positions and velocities were stored every 5 ps. The system was simulated in the NVT ensemble and temperature was held at 300 K with a Nosé-Hoover thermostat. The infinitely periodic (in x and y directions) sheet contains 1500 atoms and was simulated in a box of size [6.369 nm, 6.131 nm, 3.0 nm]. Lennard-Jones forces were calculated with a plain cut-off of 1.0 nm, and all carbon atoms were uncharged. The stored trajectories were analyzed with our custom GROMACS implementation [37] outlined in [7] to produce stress fields with a grid spacing of 0.005 nm for the IK-CFD definition. The stress is then post-processed to obtain smoother fields with a Gaussian filter of 1.25Å, barely large enough to provide smooth fields without excessively smearing out the non-uniform features (see section 2.4).

3.3 DPPC bilayer

The DPPC (1,2-dipalmitoyl-sn-glycero-3-phosphocholine) bilayers were simulated with the Berger [26] FF obtained from the website of the Tieleman group [27]. Three bilayer systems were simulated with 1) pure L-DPPC in both leaflets, 2) pure L-DPPC in the upper leaflet

and pure D-DPPC in the lower leaflet, and 3) a homogeneous mixture of L-DPPC and D-DPPC in both leaflets. Lennard-Jones forces were calculated with a plain cut-off of 1.0 nm. Long-range electrostatic interactions were computed using the particle-mesh Ewald (PME) method with a real-space cut-off of 1.0 nm and a Fourier grid spacing of 0.15 nm. Pressure was semi-isotropically coupled with a Parrinello-Rahman barostat at 1 atm, and the temperature was held constant at 323 K with a Nosé-Hoover thermostat. Each bilayer system contains 200 lipids and 12,000 SPC [28] water molecules, and the integration time step was 2 fs. Each bilayer simulation was run for a 400 ns equilibration period, followed by a 400 ns data collection period where the positions and velocities were stored every 5 ps. The stored trajectories were then analyzed to produce stress profiles using a grid spacing of 0.1 nm. Given that the current implementation does not take into account the electrostatic contributions computed in reciprocal space, the analysis of the stress from the PME method was carried out only considering Coulomb forces up to a cut-off radius of 2.2 nm. The accuracy of this common treatment has been previously examined in [7].

3.4 Coiled-coil

A synthetic coiled-coil protein was constructed from two identical parallel alpha-helices each with the amino-acid sequence (IEALKAE)₁₄. The protein was simulated as an infinitely long periodic molecule with a pitch of -3.673° per residue, so that the beginning and end residues of each chain would interact seamlessly across the periodic boundary. The positions of the backbone atoms were generated using the CCCP server [29, 30] and the sidechain positions were subsequently added with the molecular visualization package UCSF Chimera [31]. The amino-acid sequence was selected as it has been experimentally shown to be very stable even for short chains [32]. The protein was simulated with the CHARMM22/CMAP force field [52, 21]. Lennard-Jones forces were calculated using a cut-off scheme with a switching function between 1.0 nm and 1.2 nm. Long-range electrostatic interactions were computed using the particle-mesh Ewald (PME) method with a real-space cut-off of 1.2 nm and a Fourier grid spacing of 0.12 nm. Temperature was held constant at 298 K with a Nosé-Hoover thermostat. The system was composed of 196 protein residues (3,080 atoms) with 8,703 TIP3P [33] water molecules (26,109 atoms) and 28 Na⁺ ions to neutralize the protein charge. Two alpha carbons of each protein chain were harmonically restrained with a force constant of 500 kJ/mol·nm² in order to prevent rotation of the molecule. The system was simulated under constant volume conditions, with the box size ([14.423 nm, 4.488 nm, 4.488 nm]) adjusted to produce global pressures close to 1 atm. The hydrated protein system was first pre-equilibrated with harmonic position restraints on the protein backbone atoms for 250 ps. After the short pre-equilibration, the system was simulated for 300 ns where the first 100 ns were used for equilibration and the remaining 200 ns for data collection (storing position and velocities every 5 ps). The stress fields (cCFD, nCFD, and GLD) for the coiled-coil protein were calculated over the simulation period from 100 to 300 ns using a coulomb cut-off radius of 2.2 nm and a grid spacing of 0.1 nm. The computed stress fields were processed with a Gaussian filter (standard deviation of 0.8 nm) to remove high frequency fluctuations. The surface of the protein used to compute the traction was obtained as an iso-contour of the mass-density of the protein (also processed with a Gaussian filter with a standard deviation of 0.4 nm). Visualization of the traction was performed with the program ParaView.